Colloidal silver nanoparticle gradient layer prepared by drying between two walls of different wettability



2009 J. Phys.: Condens. Matter 21 264012

(http://iopscience.iop.org/0953-8984/21/26/264012)

J. Phys.: Condens. Matter **21** (2009) 264012 (8pp) doi:10.1088/0953-8984/21/26/264012

# Colloidal silver nanoparticle gradient layer prepared by drying between two walls of different wettability

**S V Roth[1,7], M Kuhlmann[1], H Walter[2], A Snigirev[3], I Snigireva[3], B Lengeler[4], C G Schroer[5], M Burghammer[3], C Riekel[3] and P Müller-Buschbaum[6,7]**

[1] HASYLAB at DESY, Notkestraße 85, D-22607 Hamburg, Germany
[2] CSEM Basel, Mattenstrasse 22, CH-4002 Basel, Switzerland
[3] ESRF, BP 220, F-38043 Grenoble Cedex, France
[4] II. Physikalisches Institut B, RWTH Aachen, Physikzentrum Seffent-Melaten, D-52074 Aachen, Germany
[5] Institut für Strukturphysik, Technische Universität Dresden, D-01062 Dresden, Germany
[6] Technische Universität München, Physikdepartment E13, James-Franck-Straße 1, D-85747 Garching, Germany

E-mail: stephan.roth@desy.de and muellerb@ph.tum.de

Received 31 October 2008, in final form 8 December 2008
Published 11 June 2009
Online at stacks.iop.org/JPhysCM/21/264012

**Abstract**
A one-dimensional silver (Ag) nanoparticle gradient layer is prepared from an aqueous colloidal solution upon a polystyrene (PS) coated silicon (Si) substrate. For preparation two walls of different wettability are used. The 40 nm PS-layer exhibits a locally constant film thickness due to the strong roughness correlation with the underlying Si-substrate and is less wettable as compared to the glass plate placed above. The Ag nanoparticles have a triangular prism-like shape. The structural characterization of the obtained complex gradient formed by drying is performed with microbeam grazing incidence small-angle x-ray scattering based on compound refractive lenses. Due to the adsorption from aqueous solution in the selective geometry a double gradient type structure defined by two areas with characteristic lateral lengths and a cross-over regime between both is observed.

## 1. Introduction

Colloidal nanoparticles are fascinating and versatile building blocks for the fabrication of two- (2D) and three-dimensional (3D) micro- and nanostructures [1], because of their uniform size, shape, composition, and properties (both surface and bulk). Recently, patterning of nanoparticles on different substrates with both long- and short-range order has started to attract strong interest in nano-science research. In particular, metal and semiconductor nanoparticles display fascinating size-dependent structural, electronic, optical, magnetic, and chemical properties, which make them promising materials to be tailored and functionalized as fundamental building blocks for emerging nanotechnology applications [2, 3]. The self-organization of such nanoparticles turned out to be a powerful tool for the construction of highly ordered colloidal crystals, biologically active substrates and optical and electronic devices [4–6].

Metal nanoparticles, which are designed to be used as an electronic ink, will be well suited for applications such as printed radio frequency identification (RFID) tags and antennas, digitally printed multilayer circuit boards, printed membrane keyboards, smart package, and electrical security devices. Colloidal nanoparticles solutions are considered to be very promising for these applications since they may potentially be fabricated entirely using printing technologies, eliminating the need for such major cost points as lithography, vacuum processing including physical vapor deposition, plasma etching, and chemical vapor deposition (CVD), while simultaneously allowing the use of reel-to-reel processing,

[7] Authors to whom any correspondence should be addressed.

 

resulting in reduced substrate handling and clean-room costs as well. Furthermore, since printing is well established, material and disposal costs are also expected to be reduced.

In particular silver and gold nanoparticles have been used for investigations related to wetting, dewetting, self-assembly/self-organization, and pattern formation of colloidal nanoparticle solutions on solid surfaces [7–17]. In addition to the nano-electronics application, silver nanoparticles are also interesting in biological applications as they are used as anti-bacterial agents or can be harnessed for their optical properties comparable to gold nanoparticles.

The optical properties of metal nanometer-sized clusters strongly differ from that of bulk matter [18–20]. The reason for these extraordinary optical properties is the so-called plasmon resonance, which occurs due to the confinement of the electron gas in small nm-sized metal clusters. These collective electron oscillations lead to strong absorption bands in the visible and infrared regime and depend on the metal used, the cluster layer structure and the morphology [21–25]. These special optical properties—compared to bulk matter—can be used for optical data storage. Information can be spectrally coded by clusters with different resonance wavelengths [22]. Hence multi-wavelength optical memory systems with a much increased storage capacity can be set up [26]. Moreover, in biodiagnostics or chemical analysis [21, 27–30] nanometer-sized noble metal clusters are used to enhance the sensitivity for biorecognition systems down to single DNA-strands and allow even for DNA-sequencing. The fluorescence intensity of single molecules attached to nm-sized gold or silver clusters is increased by several orders of magnitude, stimulated by the clusters plasmon resonance, when irradiated by a monochromatic laser beam (surface enhanced Raman spectroscopy (SERS)) [7–10]. For multi-color labeling Jin *et al* [31] offer a novel approach, namely the photoinduced conversion of spherical silver nanoclusters into nanoprisms. The ratio of nanospheres to nanoprisms depends on the irradiation time. Hence this method can be used to design sensors based on the shape of the particles. Again, this originates from the fact that the plasmon resonance strongly depends on the nanocluster size, arrangement *and* shape [32].

For a large number of the possible applications a polymer substrate is interesting [12], on the one hand due to the low costs of polymers and polymer processing which is advantageous for mass production and on the other hand due to the possibility to control the wettability by the choice of the polymer or a surface treatment of the polymer. The interaction of the metal nanoparticles with the polymer is of crucial importance for pattern formation achieved with colloidal nanoparticle solutions on polymer surfaces. Whereas pattern formation upon drying of colloidal metal nanoparticles solutions on solid supports was focused upon in several investigations [13–17] the patterns resulting from solutions which are placed between two solid walls has only rarely been addressed. In the present investigation we focus upon a water-based colloidal silver nanoparticle solution, which is in contact with two solid walls of different wettability and the achievable patterns after drying. A non-wettable polystyrene surface, on which the nanoparticles layer is formed, was countered by a wettable glass surface placed above.

In general, for a better understanding of the structure and morphology of metal cluster layers on the top of polymer films it is necessary to optimize such preparation setups. Typically, after drying, a gradient in the nanoparticles structure is installed [15, 16] which offers two advantages: (1) the installed gradient can be taken as such and used in a type of combinatorial investigation which allows one to extract special structure–property relationships as a function of the control parameter varied along the gradient. (2) The entire gradient can be taken as a desired structure for applications related to anti-counterfeiting or molecular selection in biosensors. However, with respect to a structural characterization such gradient samples are more challenging as compared to samples with a uniform structure. Standard real space characterization techniques such as atomic force microscopy (AFM) and transmission electron microscopy (TEM) will become laborious because such gradients typically extend over millimeters to centimeters. Due to the developments of micrometer and sub-micrometer-sized x-ray beams at synchrotron facilities with microbeam grazing incidence small-angle x-ray scattering ($\mu$GISAXS), an advanced scattering technique is available which allows for a local scattering experiment. As a consequence, such $\mu$GISAXS turned out to be extremely well suited for the characterization of structural gradients [13–17, 33–35].

In the present investigation $\mu$GISAXS is used for the structure characterization of the morphology along the gradient after drying of the aqueous colloidal silver nanoparticle solution. In contrast to simple adsorption experiments, a more complex gradient with two cross-over lengths is detected. It results from the imposed geometry with two confining walls. In comparison to solutions in contact with only one wall, the presence of the covering wall significantly reduces the solvent evaporation, which has an additional impact on the ordering process besides the differences in wettability.

After a brief introduction to the sample preparation and fundamentals of the experimental techniques ($\mu$GISAXS), the long ranged correlations introduced by the polymer film are discussed. Next the gradient structure is investigated. The article concludes with a summary of the recent results.

## 2. Experimental details

### 2.1. Materials

The colloidal silver nanoparticle gradient was prepared in a three-step-process. As substrates we used native oxide covered Si(100) surfaces (MEMC Electronic Materials Inc., Spartanburg). The substrate surfaces were cleaned for 15 min in an acid bath (100 ml 80% $H_2SO_4$, 35 ml $H_2O_2$ and 15 ml deionized water), then rinsed in deionized water and afterwards dried with compressed oil-free nitrogen [36]. The applied cleaning protocol was designed so as not to increase the Si surface roughness. Thin polystyrene films (molecular weight $M_w = 207\,000$ g mol$^{-1}$, molecular weight distribution $M_w/M_N = 1.02$) of nominally 40 nm thickness were spin coated onto the pre-cleaned substrates (1950 rpm for 30 s). Immediately before spin coating, the dry substrates were flushed with fresh toluene.

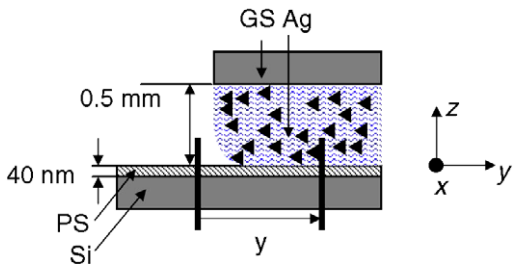


**Figure 1.** Sketch of the sample preparation. The colloidal silver nanoparticle solution (Ag nanoprisms) filled in the gap (0.5 mm) between the substrate (Si-wafer covered with 40 nm PS) and a glass slide (GS). The resulting menisci are exaggerated for clarity. The investigated part is marked with $y$.

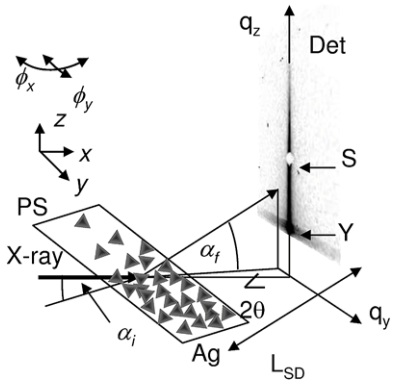


**Figure 2.** Schematic geometry of the microbeam grazing incidence small-angle x-ray scattering ($\mu$GISAXS) experiment. The sample is sketched as a gradient ($y$-direction) of triangular silver clusters. PS denotes the part of the sample with an uncoated polystyrene layer and Ag the part covered with nanoparticles. $\phi_x$, $\phi_y$ refers to the two-dimensional goniometer and $x$, $y$, $z$ to the sample translation stages. $L_{SD} = 1.17$ m is the sample-detector distance and Det denotes the high-resolution two-dimensional detector. $q_y$ and $q_z$ define reciprocal space coordinate system. The beam parameters are: diameter 5 $\mu$m, incident angle $\alpha_i = 0.813°$, wavelength $\lambda = 0.975$ Å, exit angle $\alpha_f$ and out-of-plane angle $2\theta$ (referring to the scattering plane defined by the incident and exit angles). The $x$-axis is oriented parallel to the incoming beam. S denotes the specular peak and Y the area of the Yoneda peaks in the scattering pattern.

The silver (Ag) clusters were synthesized in an aqueous solution using $AgNO_3$, trisodium citrate, $NaBH_4$ and BSPP (Bis($p$-sulfonatophenyl) phenylphosphine dihydrate dipotassium) as described by Jin *et al* [31]. After the synthesis of spherical clusters with a diameter of $D_{Ag} = 20$ nm conversion into nanoprisms was done by illuminating the solution with a halogen lamp (40 W) for three days. The UV part of the spectrum was minimized by illuminating through a 2 mm thick glass plate. After three days the color changed from yellow to green due to the change in the plasmon resonance of the nanoparticles, confirming the conversion. The concentration of the nanoparticles in solution was 0.001 wt%.

For gradient preparation via adsorption between two solid walls a higher concentration of the nanoprisms in solution was needed. Therefore, the solution was centrifuged at 18 000 rpm for 30 min. An adsorption chamber, allowing for the geometry with two different wall wettabilities, was assembled by positioning a pre-cleaned glass slide over the PS coated Si-wafer. Teflon spacers (0.5 mm in thickness) in between both PS/Si and glass were used for this purpose. The glass slide covered half of the wafer. The water contact angle of the glass surface (0°) was smaller than that of the PS surface (95°), resulting in a different wettability. Subsequently, the concentrated solution (0.01 wt%) was sucked into the adsorption chamber by capillary forces, see figure 1. Adsorption of a monolayer of Ag-clusters was allowed during 2 h of drying under ambient conditions. At the contact line of the nanoparticle solution a gradient in the Ag nanoparticle layer emerged.

### 2.2. Methods

The installed colloidal silver nanoparticle gradient was investigated using microbeam grazing incidence small-angle x-ray scattering ($\mu$GISAXS) [13–17, 33–35]. $\mu$GISAXS is a surface- and interface sensitive method. It is especially useful to investigate the above described gradient, as the nanoparticle (i.e. scattering center) concentration is low implying a low nanoparticle coverage and the distribution of the nanoparticles is inhomogeneous and extends over a large area in the range of millimeters. Due to the averaging over the footprint of the beam, $\mu$GISAXS yields a high statistical relevance of the data collected. The combinatorial investigation of the structural transitions in the gradient was performed at the beamline ID13/ESRF [37] using a wavelength $\lambda = 0.975$ Å at an incident angle of $\alpha_i = 0.813°$. The details of the experimental set-up are shown in figure 2. As focusing elements we used beryllium compound refractive lenses (BeCRL) [38]. The BeCRL allow for a similar beam size before final collimation compared to the standard optical elements used [37], but at the same time their divergence is lower, leading to an increased resolution in reciprocal space [39]. The final beam size shaping was done using a collimator, resulting in a symmetric beam size of $B = 5$ $\mu$m. The sample was mounted on a two-dimensional goniometer and an $x/y/z$-stage to allow for tilting and translation of the sample. The gradient was adjusted parallel to the $y$-axis (perpendicular to the beam). The sample was scanned through the x-ray beam with a step size of $\Delta y = 100$ $\mu$m. Though optically the inspected gradient looks like a sharp line, the $\mu$GISAXS investigation—enabled by its high sensitivity even at low nanoparticle concentrations—hints at a much larger extension, over some millimeters, due to boundary effects of the liquid interface [40–43]. The beam spot on the sample surface is elongated in the $x$-direction due to the grazing incidence geometry, showing a footprint ($y \times x$) of $5 \times 300$ $\mu$m$^2$. Thus the spatial resolution of 5 $\mu$m is preserved in the important lateral (gradient) direction. The beam is specularly and diffusely scattered from the sample surface, see figure 2. A two-dimensional high-resolution detector (MARCCD, 2048 × 2048 pixel array, pixel size 64.5 $\mu$m) records the scattered intensity. The direct and the specularly reflected beam are blocked by a lead beamstop (diameter 0.4 mm and 4 mm respectively) to avoid damage or saturation of the detector due to the intense x-ray beam. The flight path between sample and detector has been evacuated to further

reduce air scattering. The sample to detector distance was set to $L_{SD} = 1.17$ m to enable a detection of the relevant length scales. The detector coordinate system $q_y/q_z$ is related to the scattering angles as $q_z = 2\pi/\lambda\ (\sin\alpha_i + \sin\alpha_f)$ and $q_y \approx 2\pi/\lambda \sin 2\theta$, with $q_z$ and $q_y$ denoting the components of the scattering vector perpendicular and parallel to the sample surface.

In general, the off-specular (diffusely) scattered intensity in the $q_z$-direction is determined by density variations perpendicular ($z$) to the sample surface [44]. Structures in the $x$–$y$-plane lead to out-of-plane (with respect to the incoming beam and the sample surface normal) signals with finite $q_y$ and $2\theta \neq 0$. The $q_x$-component is approximately two orders of magnitude smaller than for $q_y$ and $q_z$ and can hence be neglected.

## 3. Results

After drying of the colloidal silver nanoparticle solution the installed gradient was scanned in the x-ray beam to extract the position-dependent morphology. A distance of 6000 $\mu$m was scanned in steps of $\Delta y = 100$ $\mu$m starting in the uncovered part and ending in the homogeneously covered part of the gradient (acquisition time 100 s). Due to the preparation technique used with two walls of different wettability, the gradient spans a rather large distance although optically it appears smooth and abrupt. Figure 3 shows a selection of six typical 2D $\mu$GISAXS patterns of this line scan along the gradient. The $y$-position of every tenth $\mu$ GISAXS pattern is indicated in the figure. A clear change in the diffuse scattered intensity along the gradient is visible. The zero point of the scan ($y = 0$ $\mu$m), is chosen by the marked decrease in resonant diffuse scattering (see figure 6(b)), indicating the onset of the gradient.

At $y = -1700$ $\mu$m only scattering from the homogeneous PS is recorded. In the 2D representation in figure 3 it appears weak as compared to the scattering originating from the Ag nanoparticles, because polymers typically scatter less as compared to metal nanoparticles. Along the gradient (towards larger $y$ values) the off-specular scattering increases due to the presence of the Ag nanoparticles. For data analysis selected cuts from the 2D intensity distribution were analyzed. With these cuts the vertical and horizontal structure is analyzed for the individual positions probed along the gradient.

### 3.1. Vertical structure

For the detection of correlations along the surface normal, vertical cuts from the 2D intensity (with respect to the Si surface) are suited. In these cuts at $q_y = 0$, which are frequently called detector scans, the off-specular scattered intensity in the $q_z$-direction is probed [44]. Due to the small angles involved, a variation in $q_z$ can be treated as $\alpha_i = \text{const}$ and $\alpha_f$ varying, following $\Delta q_z = 2\pi/\lambda \Delta\alpha_f \cos\alpha_f$. In the central vertical cuts the Yoneda peak [45] is one prominent feature. It arises as an interference effect of the incoming primary x-ray beam and the x-ray beam scattered at the critical angle $\alpha_f = \alpha_c$ of the probed sample. Due to the

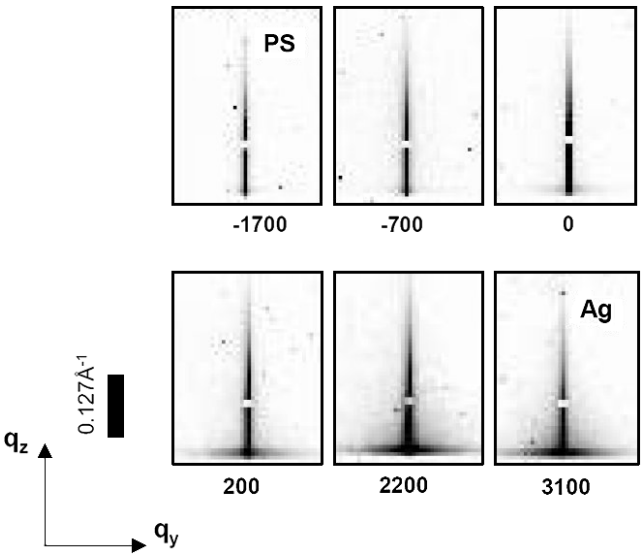


**Figure 3.** Typical 2D $\mu$GISAXS patterns of a line scan along the gradient (in the $y$-direction). The scale bar corresponds to $q = 0.127$ Å$^{-1}$. The zero point of the scan ($y = 0$ $\mu$m), is chosen by the marked decrease in resonant diffuse scattering (see figure 6(b)). The step size was $\Delta y = 100$ $\mu$m due to the large extension of the gradient. The numbers indicate the scan position of the corresponding scattering pattern.

emerging standing wave field the intensity at the critical angle is increased (maximum of the transmission function). The exact shape and position of the Yoneda peaks depends on the layer type, interface roughness and chemical composition.

Figures 4(a)–(f) show a clear change in the number and intensity of the Yoneda peaks. At $y = -1700$ $\mu$m (figure 4(a)), only the PS and Si Yoneda peak are present (pure PS-layer). Along the gradient with increasing amount of deposited Ag nanoparticles a third Yoneda peak originating from scattering due to the Ag nanoparticles emerges (e.g. at $y = 2200$ $\mu$m, figure 4(e)), leading to a strong change in the shape of the curve in range of Y.

The second prominent feature of the central vertical cuts is the oscillation in the intensity along the $q_z$ direction (see figure 4). These oscillations originate from the interference of partially coherent waves being diffusely scattered at the interfaces. The maxima of this so-called resonant diffuse scattering (RDS) indicate the distance $d_{corr}$ of the partially correlated interfaces. The RDS maxima fulfil the one-dimensional Bragg condition $\Delta q_z = 2\pi/d_{corr}$. In the present investigation the oscillations are caused by the long ranged correlations of the PS-layer and indicate the thickness of the PS-layer. The correlated distance corresponds to $d_{corr} = 40$ nm, which matches the total PS-layer thickness. Along the gradient the oscillation amplitude and the position of the maxima change (see figures 4(a) and (f)). The change in position is due to the phase shift of the scattered wave induced by the build-up of the Ag-cluster layer, leading to a shift in the exit angle $\alpha_f$. As the multilayer structure changes from Si/PS/air to Si/PS/Ag, the nature of the interfaces changes which induces a change in the refractive index and hence in the Fresnel reflectivity [46–48]. The remarkable feature, however,

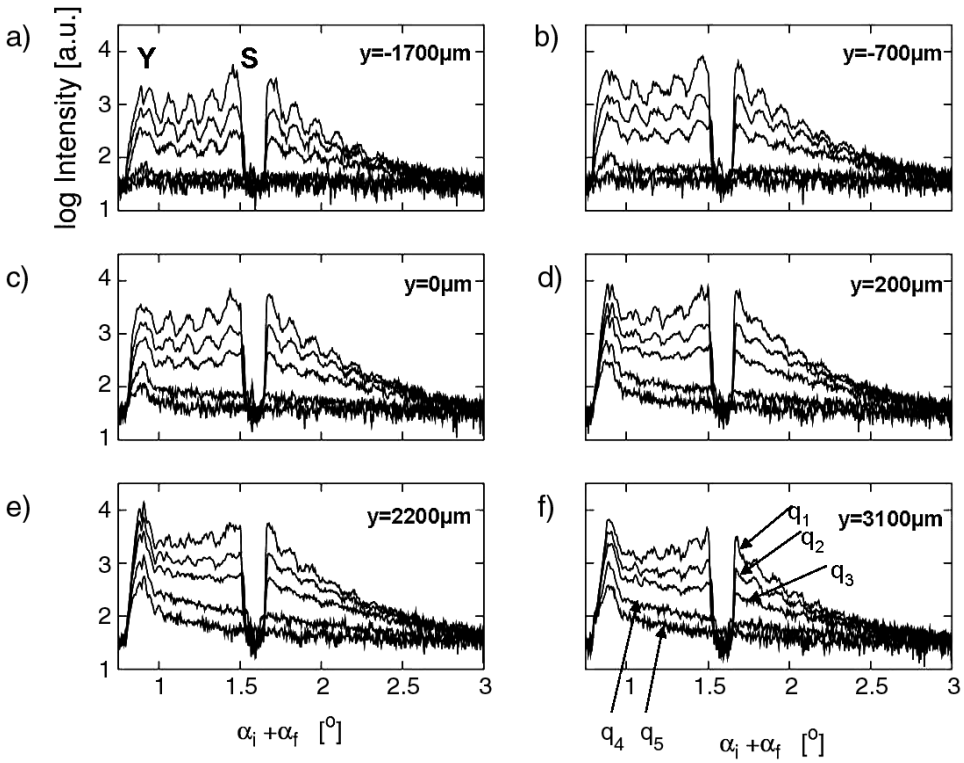


**Figure 4.** Detector ($\Delta q_y = 0$) and off-detector scans performed for 6 scan positions (a)–(f) and at different values of the scattering vector $q_y$: the curves labeled $q_{1,2,3,4,5}$ correspond to $\Delta q_y = 0\ \mathrm{nm}^{-1}$, $0.011\ \mathrm{nm}^{-1}$, $0.021\ \mathrm{nm}^{-1}$, $0.06\ \mathrm{nm}^{-1}$, $0.12\ \mathrm{nm}^{-1}$ respectively. Y denotes the region of the Yoneda peaks resulting from the Si-substrate, the PS-layer and the Ag nanoparticle layer. The change in amplitude of the resonant diffuse scattering (wiggles) is clearly visible as well as the build-up of intensity for $\Delta q_y \neq 0$ along the gradient.

is the damping of the oscillations due the presence of the Ag nanoparticle layer. This damping can be explained by the large roughness of the nanoparticle layer. During the drying process of the solution the nanoparticles are deposited without having a correlation to the structure of the homogeneous PS surface. Hence, due to the presence of the Ag nanoparticles the interface PS/Ag becomes rougher and less correlated to the PS/Si interface. The thickness of the PS-layer is not altered by the deposition process, because an aqueous colloidal solution was used and water is not swelling or penetrating into the PS-film.

In addition to the analysis of the central vertical cuts, off-central vertical cuts are analyzed. The build-up of the Ag nanoparticle layer is clearly followed in these so-called off-detector cuts, i.e. cuts along $q_z$ at finite $q_y$ ($\Delta q_y \neq 0$), see figures 4(a)–(f). At $y = -1700\ \mu$m (figure 4(a)) the intensity is concentrated in a narrow band $|q_y| \leqslant 0.0212\ \mathrm{nm}^{-1}$ along $q_z$. This position is identified with the pure PS-layer of 40 nm thickness. Already at $y = -700\ \mu$m additional diffusely scattered intensity emerges in the off-detector scan ($q_y = 6.02 \times 10^{-2}\ \mathrm{nm}^{-1}$), although the out-of-plane cuts do not reveal the presence of a most prominent in-plane length, see below and figure 6. At $y = 0\ \mu$m a strong intensity in the off-detector cuts is present clearly showing the presence of the nanoparticles on the surface.

In figure 6(b) we plotted the amplitude of the RDS fringes versus the probed position along the gradient. The RDS amplitude nearly drops by a factor of two for $y > 0\ \mu$m, indicating the loss of correlation between the interface PS/Si and Ag/PS. This is due to the fact that the adsorption process of the nanoparticles onto the PS-substrate is stochastic and shows no preferential ordering.

### *3.2. Horizontal structure*

Structures in the sample $x$–$y$-plane lead to out-of-plane (with respect to the incoming beam and the sample surface normal) signals with finite $q_y$ and $2\theta \neq 0$. Thus out-of-plane cuts from 2D intensity distribution were analyzed at $q_z = \mathrm{const}$. For each scan position along the gradient these cuts were taken close to the critical angle of PS at $\alpha_f = 0.0957°$, as due to the Yoneda peak the signal is most sensitive to the nanoscopic structure of the layers and the interfaces. Figure 5 shows two exemplary cuts representing the uncovered PS part of the gradient at $y = -1700\ \mu$m and the installed Ag nanoprism structure at $y = 3100\ \mu$m. Clearly the uncovered PS-layer ($y = -1700\ \mu$m) does not show the presence of length scales parallel to the sample surface. Due to the presence of the Ag nanoparticles on the sample surface a new horizontal length scale emerges (as indicated by the position of the arrow, $y = 3100\ \mu$m), namely the distance of the nanoclusters.

To analyze the $\mu$GISAXS data, they were fitted with the program IsGISAXS [49, 50] using the distorted wave Born approximation (DWBA). The local monodisperse approximation (LMA) was applied to account for the coupling

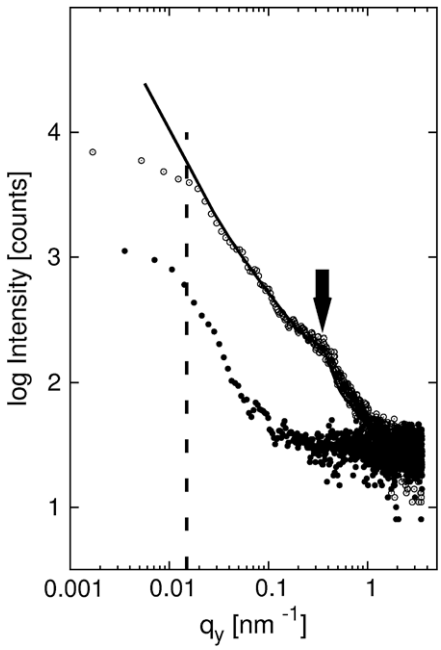


**Figure 5.** Out-of-plane scans of the pure PS-film at $y = -1700$ $\mu$m (filled circles) and of the Ag nanoprism structure at $y = 3100$ $\mu$m (open circles) for $q_z = 0.102$ Å$^{-1}$. The side maximum at $q_{y,\max}$ (marked with an arrow) indicates the most prominent in-plane length $\xi$ as a result of the build-up of the Ag nanostructure. The solid line is a fit to the data as explained in the text. The dashed line marks the resolution of the $\mu$GISAXS experiment.

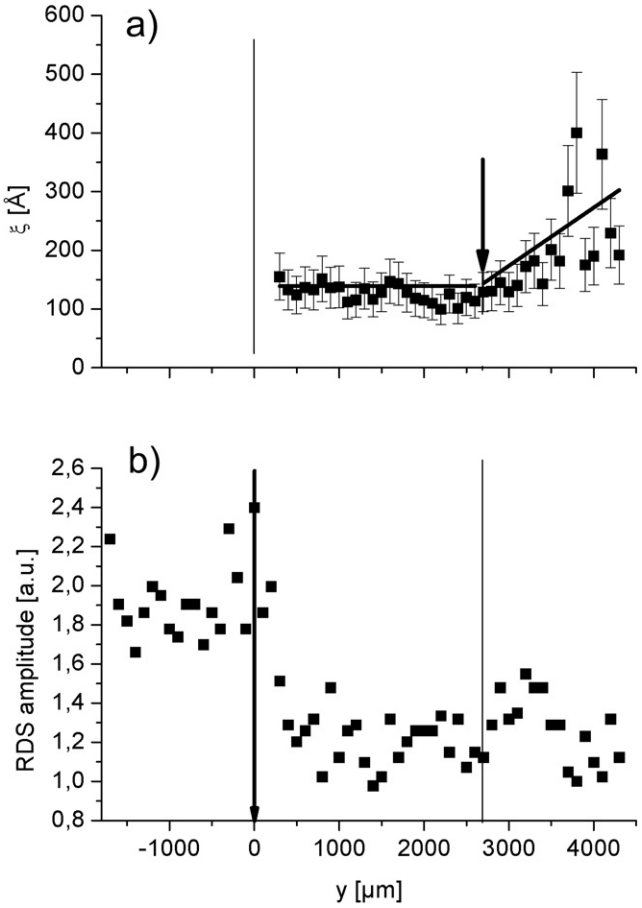


**Figure 6.** (a) Nearest neighbor distance of the deposited nanoprisms $\xi$ plotted as a function of the scan position. Note the double gradient structure: PS $\rightarrow$ Ag-layer with constant $\xi$ followed by a region of increasing $\xi$ at a position of $y = 2600$ $\mu$m indicating the end of the influence of the meniscus boundary conditions (figure 1).
(b) Resonant diffuse scattering amplitude (RDS amplitude) as a function of the scan position. The nominal zero point (vertical arrow) shows a marked decrease in the RDS amplitude due to the additional roughness induced by the Ag-layer. The arrows and the vertical lines indicate the two cross-over points.

between the position and the type of the particles [51, 52]. In LMA the scattering weight of each particle is replaced by its mean value over the size distribution and the scattering intensities from monodisperse subsystems are incoherently summed up and weighted by the size–shape probabilities. This approach requires that the modeled nanoparticle layer consists of monodisperse domains only. For modeling, different particle geometries such as spheroids, truncated spheres, cylinders and prisms were tried. The best agreement was obtained by use of the prism geometry, as expected from the type of nanoparticles used.

From the modeling of the data at the position $y = 3100$ $\mu$m we extracted a length of the prism edges $2R = 14$ nm and a height $H = 7$ nm. A Gaussian distribution of the edge length and of the height was assumed. For the edge length a quite broad distribution with $\sigma R/R = 0.5$ resulted, which explains why in the $\mu$GISAXS pattern no strong form factor signal was observed. The prism height was found to be less broadly distributed with $\sigma H/H = 0.01$. The arrangement of the nanoprisms among each other was modeled with an isotropic interference function computed from a paracrystal of hexagonal symmetry [53] averaged over all the orientations $\xi_i$. The disorder is of Gaussian type and characterized by a width $w$ to describe the loss of long-range order, i.e. the disappearing of higher-order structure factor peaks. Quantitatively, for $w/\xi \rightarrow 0$ one has crystalline order, while for $w/\xi = 1$ not even short-range order is present. From the modeling a nearest neighbor distance of the nanoprisms of $\xi = 14$ nm was determined which corresponds to the peak position in figure 5. Thus the absence of higher-order maxima results from the liquid-like disorder (width $w = 7$ nm).

The resulting parameters from all other positions show a fixed size of the nanoprisms which is in agreement with the preparation method and a change in the nearest neighbor distance $\xi$ as plotted in figure 6(a).

## 4. Discussion

Typically epitaxially grown nanoprisms show a high degree of orientation order and in the GISAXS pattern correspondingly characteristic features appear [54, 55]. However, due to the applied deposition technique based on the aqueous solution in this investigation we do not observe such orientation order. The nanoprisms have no preferential orientation and therefore no strong signal characteristic for the triangular prism-like shape of the cluster is detectable. However, from the interference function, side maxima in the $\mu$GISAXS pattern occur, which

resemble the well controlled nearest neighbor distance $\xi$ as a key control parameter. Figure 6 shows changes of this most prominent in-plane length scale as a function of the scan position. For the first scanned part of the gradient (range $-1700\ \mu\text{m} < y < 200\ \mu\text{m}$) no most prominent in-plane length scale is detectable. Because the zero point of the scan ($y = 0\ \mu\text{m}$), is chosen by the marked decrease in resonant diffuse scattering (see figure 6(b)) the range $-1700\ \mu\text{m} < y < 0\ \mu\text{m}$ corresponds to uncovered blank PS. It was shown in earlier work, that thin PS films on Si exhibit well pronounced resonant diffuse scattering [56–58]. With the onset of deposited clusters the RDS amplitude is affected (see e.g. figure 4(c)). The Ag nanoprisms contribute to the surface roughness and, as pointed out already, in their position are statistically independent from the PS surface roughness. Thus the first structured part of the gradient (range $200\ \mu\text{m} < y < 2600\ \mu\text{m}$) is on the one hand characterized by a reduced RDS amplitude and on the other hand exhibits a constant nearest neighbor distance of the Ag nanoprisms. A second structured part is given by the increase of the nearest neighbor distance for $y > 2600\ \mu\text{m}$ without a strong impact on the RDS amplitude. At the scan end ($y = 4300\ \mu\text{m}$) a plateau is reached which corresponds to the structure found for all other positions with $y \gg 4500\ \mu\text{m}$. Thus we have a transition region bridging two types of structures in the gradient.

Such cross-over from a nanoprism structure with a characteristic length on the order of 14 nm to a second regime with an increased characteristic length of 25 nm can be explained as follows. Due to the preparation process the colloidal silver nanoparticle solution is brought into an environment with two walls of different wettability (substrate/glass plate). A wettable surface allows for building up of long-range order [16, 17], whereas on non-wetting substrates, typically a loss in long-range order is observed. The force equilibrium leads to a build-up of a meniscus characterized by the two different contact angles. The curvature of the liquid interface locally alters the hydrostatic pressure and thus the local adsorption conditions. In addition, capillary forces at the three phase contact line (liquid, solid, air) tend to drive the solution in the 2D confinement, which is altered upon drying (solvent removal and movement of meniscus). These competing forces are accompanied by temperature- and concentration-gradient-driven Marangoni forces.

We conclude that only for $y > 4300\ \mu\text{m}$ the influence of the meniscus can be neglected and the adsorption onto the PS is not disturbed. An equilibrium structure results which is defined by one prominent in-plane length. Due to the newly applied geometry using a cover plate in addition to the cross-over regime a further structural equilibrated area is introduced. Over a range of approximately $2500\ \mu\text{m}$ another well defined nanoprism structure results, which is different from the one installed well between the two walls. Thus in total, a double gradient structure was achieved with the set-up using two walls, which is not available without the presence of a second limiting (top) wall.

## 5. Summary

Colloidal nanoparticles are fascinating and versatile building blocks for the fabrication of two- (2D) and three-dimensional (3D) structures. In the experiment presented here we focus on the influence of a wettability difference in the walls limiting an aqueous colloidal Ag nanoparticle solution on the structure obtained by drying. The industrial relevant preparation procedure, solution casting, was modified by adding a top wall, which was wettable by water, whereas the film onto which the nanoparticles have to be deposited was not wettable. This geometry allowed for the successful design of a more complex double gradient Ag nanoparticle structure. We were able to characterize this complex double gradient multilayer system, showing the existence of two areas which have one characteristic lateral distance and a cross-over regime separating them, by applying the advanced scattering method $\mu$GISAXS, which requires a micro-focused x-ray beam. Furthermore the penetration depth of the x-rays allowed the following of the resonant diffuse scattering of the PS-layer and the vertical correlation of the Ag nanoparticle layer along the gradient.

An immediate application will be in the field of anti-counterfeiting, due to the increased security resulting from the more complex gradient. Future investigations will concentrate on processing oriented nanostructures including two-dimensional gradients. This situation is very desirable in concerning designed two-dimensional optical elements [59], especially when gradients are introduced for property optimization [60].

## Acknowledgments

We thank G Bauer for help with the nanoparticle preparation and N Hermsdorf, J Patommel and T Titz for their assistance during the ESRF measurements. This work was financially supported by DFG in the priority program for nano and microfluidics SPP1164 (grant MU1487/2).

## References

[1] Witten T A 1999 *Rev. Mod. Phys.* **71** S367
[2] Murray C B, Kagan C R and Bawendi M G 2000 *Annu. Rev. Mater. Sci.* **30** 545
[3] Shipway A N, Katz E and Willner I 2000 *ChemPhysChem* **1** 18
[4] Aizenberg J, Black A J and Whitesides G M 1999 *Nature* **398** 495
[5] Singhvi R, Kumar A, Lopez G P, Stephanopoulos G N, Wang D I C, Whitesides G M and Ingber D E 1994 *Science* **264** 696
[6] Tzeng S-D, Lin K-J, Hu J-C, Chen L-J and Gwo S 2006 *Adv. Mater.* **18** 1147
[7] Garrell R L 1989 *Anal. Chem.* **61** 401A–11A
[8] Moskovits M 1985 *Rev. Mod. Phys.* **57** 783–826
[9] Keating C D, Kovalevski K M and Natan M J 1998 *J. Phys. Chem.* B **102** 9404–13
[10] Lecomte S, Matejka P and Baron M H 1998 *Langmuir* **14** 4373–7
[11] Biswas A, Karulkar P C, Eilers H, Grant Norton M, Skorski D, Davitt C, Greve H, Schürmann U, Zaporojtchenko V and Faupel F 2006 *Vac. Technol. Coat.* **7** 54

[12] Bauer G, Hassmann J, Walter H, Haglmüller J, Mayer C and Schalkhammer T 2003 *Nanotechnology* **14** 1289
[13] Roth S V, Burghammer M, Riekel C, Müller-Buschbaum P, Diethert A, Panagiotou P and Walter H 2003 *Appl. Phys. Lett.* **82** 1935–7
[14] Roth S V, Müller-Buschbaum P, Burghammer M, Walter H, Panagiotou P, Diethert A and Riekel C 2004 *Spectrochim. Acta* B **59** 1765
[15] Roth S V, Walter H, Burghammer M, Riekel C, Lengeler B, Schroer C, Kuhlmann M, Walther T, Sehrbrock A, Domnick R and Müller-Buschbaum P 2006 *Appl. Phys. Lett.* **88** 021910
[16] Roth S V, Müller-Buschbaum P, Timmann A, Perlich J and Gehrke R 2007 *J. Appl. Crystallogr.* **40** s346
[17] Roth S V, Autenrieth T, Grübel G, Riekel C, Burghammer M, Hengstler R, Schulz L and Müller-Buschbaum P 2007 *Appl. Phys. Lett.* **91** 091915
[18] Kreibig U and Zacharias P 1970 *Z. Phys.* **25** 128–43
[19] Dusemund B, Hoffmann A, Salzmann T, Kreibig U and Schmid G 1991 *Z. Phys.* D **20** 305–8
[20] Zeman E J and Schatz G C 1987 *J. Phys. Chem.* **91** 634–43
[21] Bauer G, Pittner F and Schalkhammer T 1999 *Mikrochim. Acta* **131** 107–14
[22] Ditlbacher H, Krenn J R, Lamprecht B, Leitner A and Aussenegg F R 2000 *Opt. Lett.* **25** 563–5
[23] Leitner A, Zhao Z, Brunner H, Aussenegg F R and Wokaun A 1993 *Appl. Opt.* **32** 102–10
[24] Hulteen J C, Patrissi C J, Miner D L, Crosthwait E R, Oberhauser E B and Martin C R 1997 *J. Phys. Chem.* B **101** 7727–31
[25] Elghanian R, Storhoff J J, Mucic R C, Letsinger R L and Mirkin C A 1997 *Science* **277** 1078–81
[26] Morinaka A, Oikawa S and Yamazaki H 1983 *Appl. Phys. Lett.* **43** 524–6
[27] Vo-Dinh T, Stokes D L, Griffin G D, Volkan M, Kim U J and Simon M I 1999 *J. Raman Spectrosc.* **30** 785–93
[28] Elghnanian R, Storhoff J L, Mucic R C, Letsinger R L and Mirkin C A 1997 *Science* **277** 1078–81
[29] Taton T A, Mirkin C A and Letsinger R L 2000 *Science* **289** 1757–60
[30] Dubertret B, Calame M and Libchaber A J 2001 *Nat. Biotechnol.* **19** 365–70
[31] Jin R, Chao Y, Mirkin C A, Kelly K L, Schatz G C and Zheng J G 2001 *Science* **294** 1901–3
[32] Hulteen J C and Van Duyne R P 1995 *J. Vac. Sci. Technol.* A **13** 1553–8
[33] Müller-Buschbaum P, Roth S V, Burghammer M, Diethert A, Panagiotou P and Riekel C 2003 *Europhys. Lett.* **61** 639
[34] Müller-Buschbaum P, Hermsdorf N, Roth S V, Wiedersich J, Cunis S and Gehrke R 2004 *Spectrochim. Acta* B **59** 1789
[35] Müller-Buschbaum P, Bauer E, Wunnicke O and Stamm M 2005 *J. Phys.: Condens. Matter* **17** S363
[36] Müller-Buschbaum P 2003 *Eur. Phys. J.* E **12** 443–8
[37] Riekel C 2000 *Rep. Prog. Phys.* **63** 233
[38] Lengeler B, Schroer C G, Kuhlmann M, Brenner B, Günzler T F, Kurapova O, Zontone F, Snigirev A and Snigireva I 2005 *J. Phys. D: Appl. Phys.* **38** A218
[39] Roth S V, Döhrmann R, Dommach M, Kuhlmann M, Kröger I, Gehrke R, Walter H, Schroer C, Lengeler B and Müller-Buschbaum P 2006 *Rev. Sci. Instrum.* **77** 085106
[40] Cazabat A M 1990 *Liquids at Interfaces* (*Les Houches Session Series*) ed J Charvolin, J F Joanny and J Zinn-Justin (Amsterdam: Elsevier)
[41] Findenegg G H and Herminghaus S 1997 *Curr. Opin. Colloid Interface Sci.* **2** 301
[42] Bührle J, Herminghaus S and Mugele F 2002 *Langmuir* **18** 9771–7
[43] Müller-Buschbaum P 2003 *J. Phys.: Condens. Matter* **15** R1549
[44] Müller-Buschbaum P 2003 *Anal. Bioanal. Chem.* **376** 3
[45] Yoneda Y 1963 *Phys. Rev.* **131** 2010–3
[46] Daillant J and Belorgey O 1992 *J. Chem. Phys.* **97** 5824
[47] Holy V and Baumbach T 1994 *Phys. Rev.* B **49** 10668
[48] Salditt T, Metzger T H, Peisl J and Goerigk G 1995 *J. Phys. D: Appl. Phys.* **28** A236
[49] Lazzari R 2002 *J. Appl. Crystallogr.* **35** 406
[50] The program IsGISAXS with instructions is available on simple request to the author R. Lazzari http://www.insp.jussieu.fr/axe2/Oxydes/IsGISAXS/isgisaxs.htm or at http://www.esrf.fr
[51] Pedersen J S 1994 *J. Appl. Crystallogr.* **27** 595
[52] Revenant C, Leroy F, Renaud G, Lazzari R, Letoublon A and Madey T 2007 *Surf. Sci.* **601** 3431
[53] Hosemann R, Vogel W and Weick D 1981 *Acta Crystallogr.* A **37** 85
[54] Stangl J, Holý V, Mikulik P, Bauer G, Kegel I, Metzger T H, Schmidt O G, Lange C and Eberl K 1999 *Appl. Phys. Lett.* **74** 3785
[55] Metzger T H, Kegel I, Paniago R and Peisl J 1999 *J. Phys. D: Appl. Phys.* **32** A202
[56] Müller-Buschbaum P and Stamm M 1998 *Macromolecules* **31** 3686
[57] Müller-Buschbaum P, Gutmann J S, Lorenz C, Schmitt T and Stamm M 1998 *Macromolecules* **31** 9265
[58] Müller-Buschbaum P, Gutmann J S, Kraus J, Walter H and Stamm M 2000 *Macromolecules* **33** 569
[59] Xia Y, Gates B, Yin Y and Lu Y 2000 *Adv. Mater.* **12** 693–713
[60] Bhat R R, Fischer D A and Genzer J 2002 *Langmuir* **18** 5640–3